Full length article

Influence of working parameters on multi-shot femtosecond laser surface ablation of lithium niobate

Felice Alberto Sfregola [a,b,*], Raffaele De Palo [a,b], Caterina Gaudiuso [a,b], Francesco Paolo Mezzapesa [a,b], Pietro Patimisco [a,c], Antonio Ancona [a,b], Annalisa Volpe [a,b]

[a] *Dipartimento Interateneo di Fisica, Università Degli Studi di Bari, Bari, Italy*
[b] *CNR-IFN UOS BARI, Via Amendola 173, Bari, Italy*
[c] *PolySense Innovations Srl, Via Amendola 173, Bari 70126, Italy*

ABSTRACT

This paper presents an experimental investigation on the ultrashort pulsed laser ablation of 128° Y-cut Lithium Niobate (LiNbO$_3$) using multi-shot fs-laser pulses at different pulse repetition frequencies (1, 10 and 100 kHz). The ablation threshold fluence was observed to rapidly decrease as the number N of incident laser pulses increased, regardless of the repetition frequency. This behavior, compatible with the incubation effect, was accurately modeled by a power law. The calculated single pulse ablation threshold $F_{th,1} = 1.98 \pm 0.15\,\mathrm{J/cm^2}$ is consistent with values reported in existing literature. The incubation coefficient S^* appears to be independent of the repetition frequencies. In contrast, the asymptotic ablation threshold $F_{th,\infty}$ decreased as the repetition frequency was increased. The study delves deeper into the impact of laser operational variables, including pulse energy, repetition frequency, total pulse count, and scanning speed, on the surface roughness and milled depth of fs-laser micromilled zones on LiNbO$_3$ substrates. A discernible trade-off between achieving control over the obtained depth and the surface finish of the process was identified, providing valuable insights for achieving precise control over fs-laser processing of LiNbO$_3$ surfaces.

1. Introduction

Lithium Niobate (LiNbO$_3$) is an artificial piezoelectric crystalline material with a wide range of applications due to its unique combination of physical properties. At room temperature, it is a ferroelectric crystal with a rhombohedral (trigonal) structure and belongs to the space group R3c, with a point group of 3 m [1]. Its chemical stability and Curie temperature of 1142 °C ensure that it remains intact even in demanding environments [2].

One of the standout features of LiNbO$_3$ is its large electro-mechanical coupling coefficients, several times larger than those of quartz. This property makes it a material of interest for the fabrication of transducer devices. For instance, LiNbO$_3$ tuning forks (LiNTFs) have already been largely employed as viscosity and density sensors for fluid properties measurements [3,4] and recently as piezoelectric transduces in Lithium Niobate-enhanced Photoacoustic Spectroscopy (LiNPAS) [5]. Furthermore, LiNbO$_3$ exhibits very low acoustic losses, which makes it an ideal candidate as the substrate of surface acoustic wave (SAW) devices. In microfluidics, LiNbO$_3$ substrates have been employed in micro-mixers [6] and in particle sorting systems based on acoustophoresis [7].

Despite these remarkable properties, the processing of LiNbO$_3$ presents challenges due to its low toughness, high anisotropy, and chemical inactivity. Various manufacturing techniques, such as diamond micro-milling [8], high precision Computerized Numerical Control (CNC) machining [9], wet and dry etching, including focused ion beam (FIB) milling [10], have been explored for the micromachining of micro-features. However, these methods often have limited processing resolution or low material removal rate resulting in time-consuming and expensive processes that constraints optimization in prototyping [11]. Femtosecond laser micromachining (FLM) addresses these drawbacks by enabling direct microstructuring of substrates without the need for preliminary chemical treatment or photomasks. FLM operates in a non-contact and chemical-free way, eliminating the risks of introducing contaminants or altering material properties through chemical interactions. These characteristics aligns with the demands of modern microfluidic device fabrication, which emphasizes simplicity and

---

* Corresponding author.
  E-mail address: felice.sfregola@uniba.it (F.A. Sfregola).

flexibility in design optimization [12,13]. Surface micromachining employing FLM has been reported for several materials, including polymers [14], composites [15], ceramics [16] and metals [17]. FLM has also found application for the fabrication of LiNbO$_3$-based microfluidic devices [18,19], as well as microresonators for medical [21] and photonics [22] applications.

Femtosecond (fs) lasers operate by emitting ultrashort pulses of light, enabling the deposition of energy in a timescale shorter than the typical lifetime of thermal relaxation processes in materials. This rapid and intense energy deposition leads to a highly localized and controlled laser-matter interaction mostly governed by nonlinear absorption phenomena, which permit to tailor processing of materials at extremely high precision.

Over the past three decades, the dynamics of fs-laser interactions with matter have been extensively studied and well documented [22]. It has been demonstrated that the quality and efficiency of FLM in transparent materials depend on both the material's properties – including composition, crystalline structure, thermal conductivity, and optical characteristics – as well as the laser parameters such as pulse duration, pulse energy, and the focusing numerical aperture [23]. However, a complete and universal understanding of the involved physical phenomena remains elusive especially when dealing with wide bandgap transparent dielectrics.

Chen et al. [24] have studied the surface-damage threshold of LiNbO$_3$ after single- and multiple fs-laser pulse irradiation. Furthermore, a prediction model for the damage threshold has been proposed by Meng et al. [25]. Fissi et al. [26] investigated the impact of changing several laser operating parameters on the microstructuring of piezoelectric substrates, including LiNbO$_3$, with a picosecond laser. However, the existing literature lacks precise and complete information on the influence of laser parameters during multi-pulse fs-laser surface ablation of LiNbO$_3$. To address this gap, in this paper, a systematic study of the response of 128° Y-cut LiNbO$_3$ during FLM was carried out.

Firstly, the laser surface ablation threshold of LiNbO$_3$ was investigated. The paper further explores the influence of laser working parameters, such as pulse energy, repetition frequency, total number of pulses, and scanning velocity, on both surface roughness and milled depth of fs-laser micromilled areas on LiNbO$_3$ substrates. Morphological analysis of processed surfaces enabled the evaluation of surface roughness and edge quality under various operating conditions.

2. Materials and methods

2.1. Materials

The substrates used in this work consist of double polished 128° Y-cut Lithium Niobate wafers (from Nano Quarz Wafer GmbH) with an area of $24.5 \times 24.5\,mm^2$ and a thickness of 500 μm. The polished surfaces have a roughness (R_a) of less than 1 nm, while the edges are in their as-cut state.

The 128° Y-cut in LiNbO$_3$ is widely used for the fabrication of acoustophoresis-based microfluidic devices [6]. Specifically, this particular cut enables the propagation of Rayleigh waves at an increased velocity, increasing from 3488 m/s of the uncut crystal to 3979 m/s. This characteristic is essential for efficient particle sorting. Furthermore, the electromechanical coupling constant for this cut ($K^2 = 5.5\%$) is much higher than that for the Rayleigh waves generated in quartz (0.16%), zinc oxide (1.1%) or aluminum nitride crystal (0.4%) [6].

2.2. Experimental setup

The set-up employed for the study of the laser ablation threshold and the influence of the laser working parameters on the laser milled depth and surface roughness is schematically shown in Fig. 1.

The light source employed was a femtosecond solid state laser system PHAROS SP 1.5 from Light Conversion. This versatile laser system offers a wide range of tunable parameters including pulse duration τ_P ranging from 100 fs to 20 ps, repetition frequency f_r from single shot up to 1 MHz, pulse energy E_P up to 1.5 mJ, and average power up to 6 W. The nominal central wavelength is 1030 nm. At the output, the laser beam is almost diffraction-limited ($M^2 = 1.3$) and linearly polarized.

The pulse duration was fixed at 200 fs during the investigation. The pulse energy was finely tuned by a half-waveplate and a polarizer, that was oriented in order to select the P component of light polarization.

The linearly polarized beam was focused and scanned onto the target surface through a PC-controlled galvo scanner (IntelliSCANN 14 from SCAN-LAB,) equipped with a f-theta lens of 100 mm focal length. The LiNbO$_3$ sample was fixed on a 3-axis manual linear translation stage (resolution 1 μm), to facilitate the positioning of the sample at the center of the working area of the scan head as well as at the focal plane of the f-theta lens.

The micromachined samples underwent a cleaning procedure, consisting of a 15-minute cycle in an isopropyl alcohol ultrasonic bath, to remove any residues left from the ablation process.

The morphological characterization of the laser machined samples
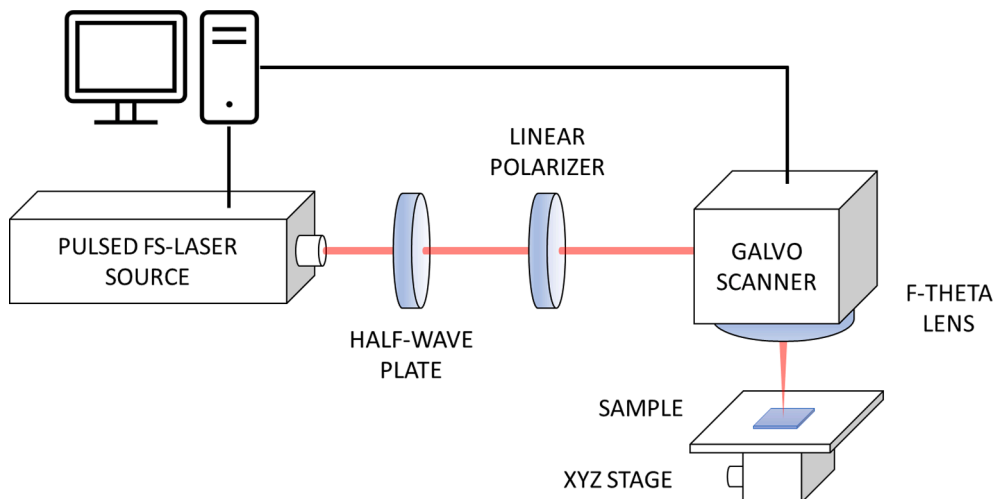
Fig. 1. Schematic of the experimental setup. The laser source and the galvo scanner are controlled by an external PC. The sample holder is provided with an XYZ linear translation stage.

was performed employing an optical microscope (Nikon Eclipse ME600) as well as an optical profilometer (Bruker ContourGT InMotion). This interferometry-based microscope offers non-contact, three-dimensional surface measurements of features within the height range from 0.1 nm to 10 mm. The built-in analysis software also allows the measurement surface roughness and step heights.

2.3. Surface ablation threshold study

The laser surface ablation threshold study of LiNbO$_3$ was carried out applying the Liu's method [27]. This well-established method based on crater analyses relates the threshold fluence $F_{th}(N)$ for N consecutive laser pulses to the crater squared diameter D^2 through the following equation:

$$D^2 = 2w^2 \ln\left(\frac{F_0}{F_{th}(N)}\right) \quad (1)$$

where F_0 is the peak laser fluence defined as:

$$F_0 = \frac{2E_P}{\pi w^2} \quad (2)$$

and w is the $1/e^2$ Gaussian beam radius.

Combining Eq. (1) and Eq. (2), the squared diameters D^2 can be linearly fitted as a function of the logarithm of the pulse energy E_P. The laser Gaussian beam radius is given by the slope $2w^2$, and the multi-pulse threshold fluence $F_{th}(N)$ can be calculated from the ordinate-intercept of the fitting line.

In this study, three sets of ablation craters – composed by 11 matrices – were generated at a different repetition frequencies f_r. In each matrix the number of pulses N is fixed, while each row is ablated with increasing pulse energy E_P. The laser working parameters for each set, matrix and row are reported in Table 1.

The morphological analysis of the ablated craters was performed using the optical microscope 's acquisition software.

It's worth noticing that the crater shapes may deviate from perfect circles. This discrepancy could be attributed to several factors: the beam's non-ideal Gaussian nature ($M^2 > 1$), a non-perfect focusing of the beam on the sample surface, or a slight telecentricity error. To account for this variability, both the minor and major axes of the elliptical crater profiles were measured. Then, the crater's diameter was subsequently determined as the average of these two measurements.

The diameter D in Eq. (1) was determined for each pulse energy E_P by averaging four diameter measurements to increase both the accuracy and the precision of the measurement. An uncertainty of 1 μm was considered to account for the maximum resolution of the image analysis software.

2.4. Laser micromilling study

The impact of the main laser process parameters on the depth and the surface roughness S_q [28] of the laser-micromilled areas has been investigated. Table 2 reports the examined parameters, including the peak fluence F_0, the pulse repetition frequency f_r, the scanning speed v_s, and the spacing between consecutive scanning lines, i.e., the hatch distance h. For each set of parameters, a pocket of $150 \times 150 \, \mu m^2$ was micromachined.

Table 1
Laser working parameters during the surface ablation threshold study.

Repetition frequency f_r [kHz]	1 – 10 – 100
Number of pulses N [-]	5 – 10 – 20 – 50 – 100 – 200 – 500 – 1000 – 2000 – 5000 – 10,000
Pulse energy E_P [μJ]	10 – 15 – 20 – 25

Table 2
Laser working parameters during the micromilling study.

Repetition frequency f_r [kHz]	1 – 10 – 100
Peak fluence F_0 [J/cm^2]	0.66 – 0.99 – 1.32 – 1.66 – 1.99 – 2.32 – 2.65 – 2.98 – 3.31 – 3.64
Scanning speed v_s [mm/s]	160 – 64 – 32 – 16 – 6 – 3 – 2
Hatch distance h [μm]	3.2 – 6.4 – 9.6 – 12.8 – 16 – 19.2 – 22.4 – 25.6 – 28.8
Scanning line overlap LO [%]	10 – 20 – 30 – 40 – 50 – 60 – 70 – 80 – 90

The pulse repetition frequency f_r and scanning speed v_s determine the laser pulse overlap PO of consecutive laser pulses along the scanning direction according to the following equation [29]:

$$PO(\%) = \left(1 - \frac{v_s}{2w \bullet f_r}\right) \times 100 \quad (3)$$

Precise control of laser pulse overlap is crucial to evenly distribute the laser energy over the machined surface, preventing excessive heating and material damage. A visual representation of the overlap of two consecutive laser pulses with a Gaussian profile can be found in Fig. 2.

The study on the laser surface ablation threshold of LiNbO$_3$ already provided insights into the material's response to different repletion frequencies and the number of incident pulses N. Therefore, instead of laser pulse overlap, it is more convenient to rewrite Eq. (3) in terms of the number of pulses N_P^{1D} irradiated on a dimensionless spot of the surface along a line scan per spot, calculated as [30]:

$$N_P^{1D} = \frac{2w \bullet f_r}{v_s} \quad (4)$$

where w was evaluated following the Liu's method.

The scanning line overlap LO of two consecutive laser spots belonging to adjacent scanning lines can be calculated as [29]:

$$LO(\%) = \left(1 - \frac{h}{2w}\right) \times 100 \quad (5)$$

where h is the distance between consecutive scanning lines.

It is insightful to rewrite Eq. (5) in terms of the number of pulses per spot N_P^{2D} that accounts for both the laser pulse and scanning line overlap, so that [30]:
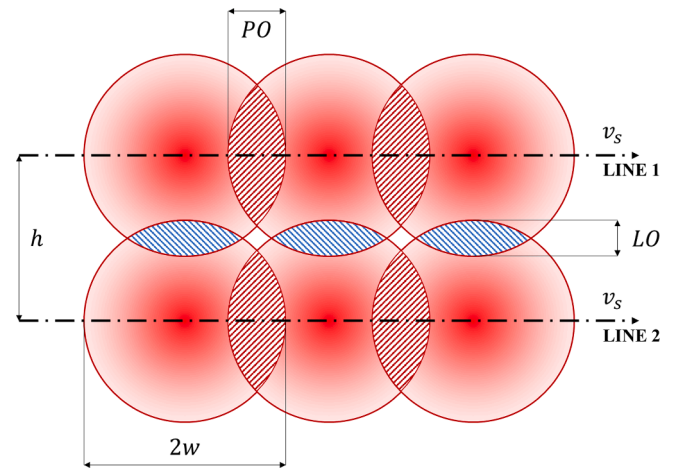
Fig. 2. Laser pulse overlap area PO (red stripes) of two consecutive laser pulses along the scanning direction. Scanning line overlap area LO (blue stripes) of two adjacent scanning lines in the laser micromilling process. The pulse energy distribution is assumed to be Gaussian. (For interpretation of the references to colour in this figure legend, the reader is referred to the web version of this article.)

$$N_P^{2D} = N_P^{1D} \frac{2w}{h} = \frac{(2w)^2 \bullet f_r}{v_s \bullet h} \qquad (6)$$

Finally, the cross-hatch scanning strategy displayed in Fig. 3 was adopted due to its enhanced machining quality and reduced roughness compared to circular patterns and parallel lines [31]. This approach ensures an even distribution of energy across successive passes of the laser beam in a grid pattern.

3. Results and discussion

3.1. Surface ablation threshold fluence and incubation

The multi-pulse threshold fluence $F_{th}(N)$ was calculated for each number of pulses N and repetition frequency f_r following the Liu's method described in Section 2.3. As representative, Fig. 4 shows the semi-logarithmic plots obtained for $N = 5, 10, 20, 50,$ and 10000 at $f_r = 10$ kHz. The fitting of experimental data with Eq. (1) returns the estimation of the Gaussian laser beam radius on the surface $w = 17.0 \pm 0.9$ μm. This value is compatible with the calculated beam waist in air, which was 16 μm.

The plot clearly shows that the diameter D of the craters increases with both the pulse energy E_P and the number of pulses N, however a saturation point is reached beyond $N = 50$. The observed behavior is well consistent with the theory of damage and/or deformation accumulation mechanisms in multi-shots irradiation [32].

Fig. 5 shows the multi-shots threshold fluence $F_{th}(N)$ as a function of the number N of applied laser shots at (a) $f_r = 1$ kHz, (b) 10 kHz, and (c) 100 kHz. The experimental data was analyzed employing three incubation models which describe the relationship between the multi-pulse ablation threshold $F_{th}(N)$ and the single-pulse threshold $F_{th,1}$.

The experimental results reveal a similar trend across all three repetition frequencies. Initially, as the number N of laser pulses increases, there is a rapid decrease of the multi-pulse ablation threshold fluence. This decrease is most significant for $N < 100$, where the threshold fluence is almost halved. For $N > 100$, the multi-pulse ablation threshold fluence F_{th} tends to a plateau level. In other words, the cumulative effects reach a saturation point: a further increase in the number of laser shots does not significantly reduce the threshold fluence. This behavior is well known in literature as incubation [33] and, refers to the progressive reduction in the ablation threshold with successive pulses, a behavior not observed in the single-pulse regime [32].

This phenomenon has been widely observed across various materials, ranging from metals, such as steel [34], copper and iron [35], to semiconductors [36], as well as dielectrics [37], such as quartz [33]. For all these materials, the observed trend indicates that the material's optical absorption increases progressively pulse after pulse, leading to
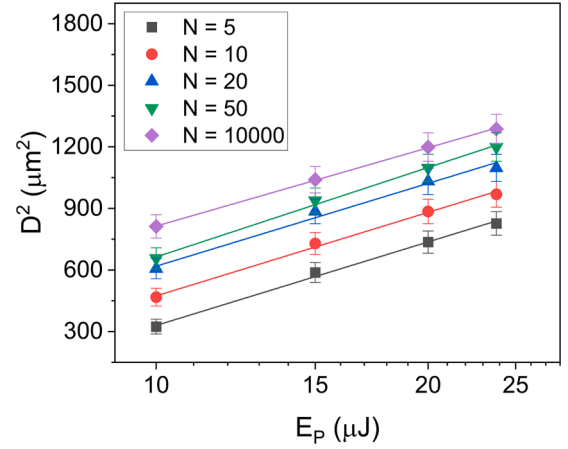

Fig. 4. Squared diameter D^2 of the ablated craters versus the pulse energy E_P semi-logarithmic plots for number of pulses $N = 5, 10, 20, 50$ and 10000 at the repetition frequency $f_r = 10$ kHz. The experimental data are fitted with Eq. (1).

enhanced excitation of free carriers with different physical mechanisms depending on the kind of material [38]. The progressive accumulation of excitation energy ultimately contributes to a reduction of the threshold for material removal [39].

The exact mechanisms underlying the incubation effect are not yet fully understood and remain a subject of ongoing research. For dielectrics, the emergence of the incubation effect is closely linked to the formation of self-trapped excitons (STEs), electron-hole pairs that become bound due to Coulomb attraction [40]. STEs can induce localized lattice rearrangements and accumulation of defects that contribute to an increase of the material's optical absorption. As a result, energy of subsequent laser pulses is absorbed more efficiently, ultimately leading to the reduction of the ablation threshold [41].

Model (1) was proposed for the first time by Jee et al. [32] and is based on the following power law:

$$F_{th}(N) = F_{th,1} N^{S-1} \qquad (7)$$

where S is an empirical parameter known as incubation coefficient which quantifies the strength of the incubation in the target material and is bound between 0 and 1. If $S = 1$, incubation is absent and the ablation threshold is not dependent from N. For $S < 1$, incubation takes place: the closer S is to zero, the faster the ablation threshold decreases. According to Model (1), the multi-pulse threshold fluence $F_{th}(N)$ should approach zero as far as the number of laser pulses becomes significantly high. Therefore, as it can be noticed in Fig. 5 (red dotted curve), Model (1) cannot accurately fit the experimental data point in the saturation
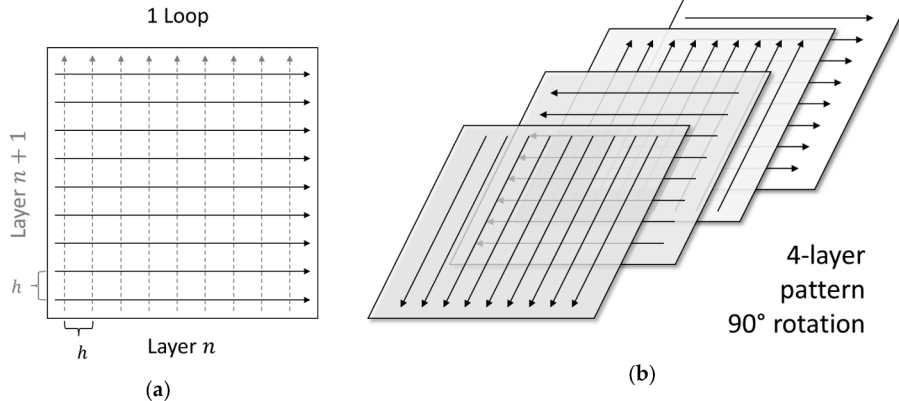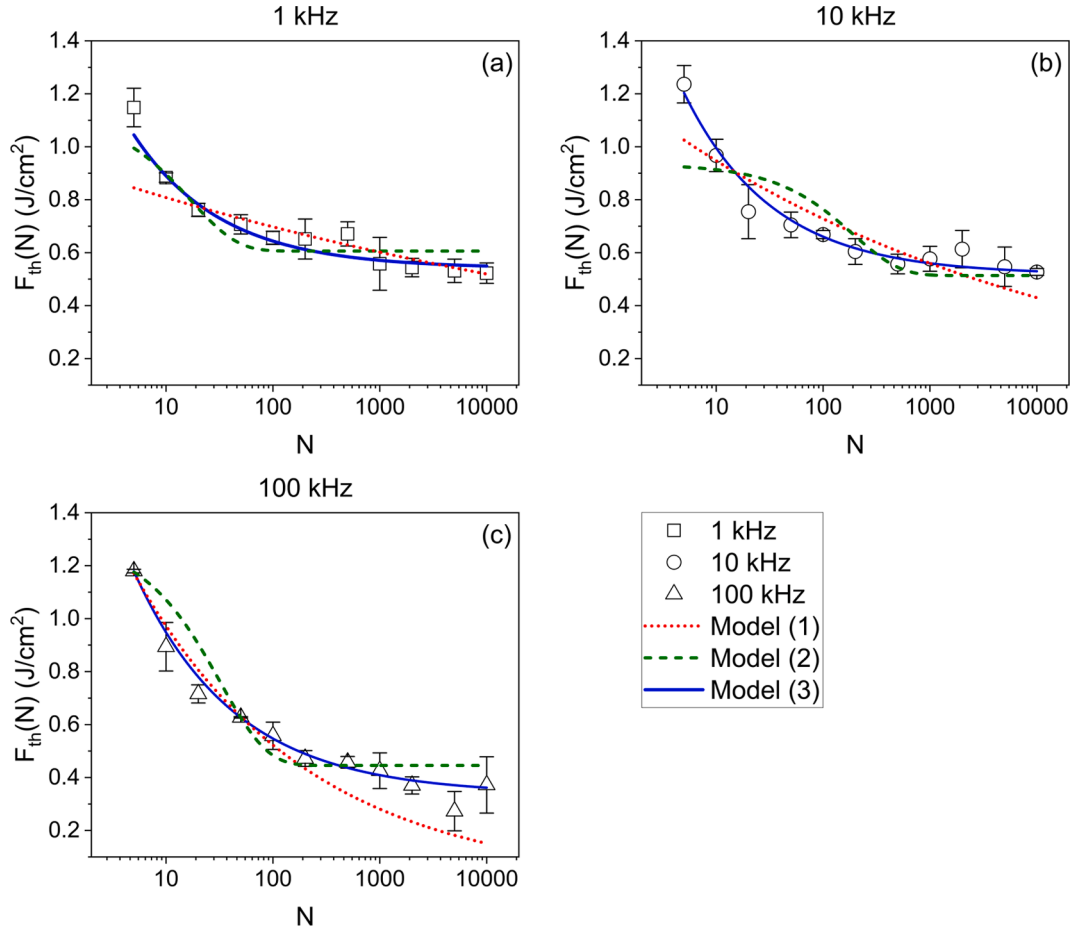

Fig. 3. Schematic of the cross-hatch scanning strategy: (**a**) The scanning lines of subsequent layers are perpendicular to each other, with a constant hatch spacing for each layer; (**b**) Each layer is obtained by rotating the previous layer counterclockwise by 90°.

Fig. 5. Multi-pulse threshold fluence $F_{th}(N)$ as a function of the number of laser pulses N, at repetition frequency f_r of: (**a**) 1 kHz, (**b**) 10 kHz and (**c**) 100 kHz. The experimental data are fitted with Model (1) (red dotted line), Model (2) (green dashed line) and Model (3) (blue solid line). (For interpretation of the references to colour in this figure legend, the reader is referred to the web version of this article.)

region for all three repetition frequencies investigated. The R-Squared values obtained by the fitting of the data with Model (1) are reported in Table 3, along with other computed parameters such as the single pulse threshold fluence and the incubation coefficient.

The saturation regime can be described by introducing a constant asymptotic fluence threshold $F_{th,\infty}$. As the number of laser pulses tends towards infinity, the multi-pulse ablation threshold converges toward this finite value instead of reaching zero.

Model (2), proposed by Rosenfeld et al. [42], is based on these considerations and follows an exponential law:

$$F_{th}(N) = F_{th,\infty} + \left[F_{th,1} - F_{th,\infty} \right] e^{-k(N-1)} \tag{8}$$

where the factor k serves a role like the incubation coefficient S of Model (1), but it is not constrained in the range $0-1$. Instead, k can take on any value depending on the extent of the incubation effect in the material. The larger k is, the fewer laser shots N are necessary to reach saturation.

Model (2) has been proven to accurately describe the incubation effect in dielectrics such as fused silica [43] and quartz [33]. The green dashed curve in Fig. 5 represents the best fit of the experimental data

acquired in the present work on LiNbO$_3$ employing Eq. (8). As it can be noticed, Model (2) better fits the data points especially in the saturation region resulting in higher R-squared values for $N > 100$ compared to Model (1) (see Table 4). Nevertheless, significant discrepancies can still be seen between the model and the experimental data in the region $10 < N < 100$ for all the repetition frequencies investigated.

Model (3), introduced by Di Niso et al. [34], is a recently proposed incubation model that takes into account both the power law formulation from Model (1) and the saturation of the threshold fluence for increasing number of pulses:

$$F_{th}(N) = F_{th,\infty} + \left[F_{th,1} - F_{th,\infty} \right] N^{S^*-1} \tag{9}$$

where S^* is a modified incubation coefficient.

This model accurately describes the entire trend of the multi-pulse threshold F_{th} from fewer number of pulses ($N < 100$) up to the saturation region, as shown in Fig. 5 (blue solid curve). Table 5 reports the results of the fitting of the experimental data with Model (3). The very high R-squared values indicate the superior accuracy of Model (3) to describe the incubation effect for LiNbO$_3$ in comparison to the other

Table 3
Results of the Model (1) fits performed at the 3 repetition frequencies.

f_r [kHz]	$F_{th,1}$ [J/cm^2]	S [-]	R^2
1	1.05 ± 0.05	0.91 ± 0.01	0.864
10	0.98 ± 0.09	0.93 ± 0.01	0.710
100	1.81 ± 0.05	0.73 ± 0.01	0.988

Table 4
Results of the Model (2) fits performed at the 3 repetition frequencies.

f_r [kHz]	$F_{th,\infty}$ [J/cm^2]	$F_{th,1}$ [J/cm^2]	k [-]	R^2
1	0.61 ± 0.03	1.10 ± 0.13	0.06 ± 0.03	0.839
10	0.54 ± 0.02	1.09 ± 0.08	0.02 ± 0.03	0.870
100	0.45 ± 0.04	1.27 ± 0.05	0.03 ± 0.03	0.990

Table 5
Results of the Model (3) fits performed at the 3 repetition frequencies.

f_r [kHz]	$F_{th,\infty}$ [J/cm^2]	$F_{th,1}$ [J/cm^2]	S^* [-]	R^2
1	0.54 ± 0.03	1.72 ± 0.26	0.47 ± 0.11	0.950
10	0.52 ± 0.01	2.11 ± 0.16	0.48 ± 0.04	0.997
100	0.34 ± 0.03	2.11 ± 0.05	0.54 ± 0.03	0.999

existing models, at least in the range of laser parameters investigated in the present work.

The fitting results indicate also that the single-shot threshold $\overline{F}_{th,1}$ appears to be independent of the repetition frequency. This observation allows the calculation of an average value, resulting in $\overline{F}_{th,1} = 1.98 \pm 0.15\,\text{J/cm}^2$. This value is compatible with the single-shot ablation threshold ($2.82\,\text{J/cm}^2$) found by Chen et al. [24] using 80 fs-pulses at $f_r = 1$ kHz. The influence of the repetition frequency on the modified incubation coefficient S^* can be also considered negligible, as the fitted values are compatible within their respective errors.

The asymptotic threshold $F_{th,\infty}$ at $f_r = 1$ kHz and 10 kHz ($0.54 \pm 0.03\,\text{J/cm}^2$ and $0.52 \pm 0.01\,\text{J/cm}^2$, respectively) is compatible with the value $0.52 \pm 0.06\,\text{J/cm}^2$ found by Chen et al. [24] employing 80 fs-pulses, while it drops to $0.34 \pm 0.03\,\text{J/cm}^2$ at $f_r = 100$ kHz. These results give some insight on the dependence of the ablation threshold of LiNbO$_3$ with the repetition frequency in the multi-shot regime, however a full characterization of $F_{th,\infty}$ as a function of f_r is beyond the purpose of this paper.

Based on the findings obtained from the laser surface ablation threshold study, further insights can be gleaned regarding the dependence of the crater's morphology on the pulse energy E_P, the repetition frequency f_r and the number of incident pulses N. As show in Fig. 6 (a-b) for $N = 500$ and $E_p = 20\,\mu$J, the crater quality is reliable both at 1 kHz and 10 kHz. Similar results are observed for all other combinations of energy and number of pulses. Conversely, increasing the repetition frequency to 100 kHz, for a large number of pulses the crater reveals the presence of chips due to excessive thermal stress on the surface [44], as shown in Fig. 6(c).

Given that the 10-kHz repetition frequency improved process efficiency compared to the $f_r = 1$ kHz case without compromising the quality of the crater's edges, we chose to keep the repetition frequency fixed at 10 kHz thereafter.

3.2. Influence of the laser parameters on the micromicromilled areas

The influence of the incident laser fluence on the milled depth was investigated at fixed scanning line overlap $LO = 50\%$ and pulses per spot $N_P^{2D} = 100$ as starting parameters. The peak laser fluence F_0 was calculated based on the pulse energy E_P using Eq. (2), while the scanning velocity v_s was determined using Eq. (4), setting 50 pulses per spot.
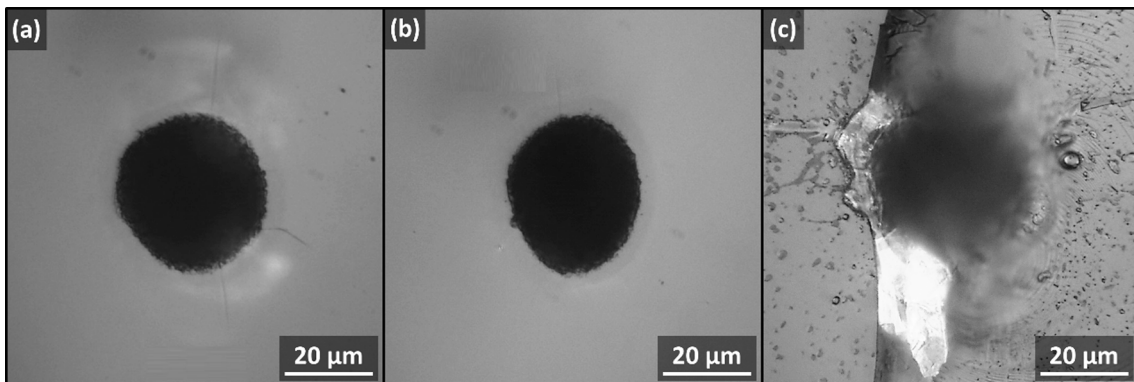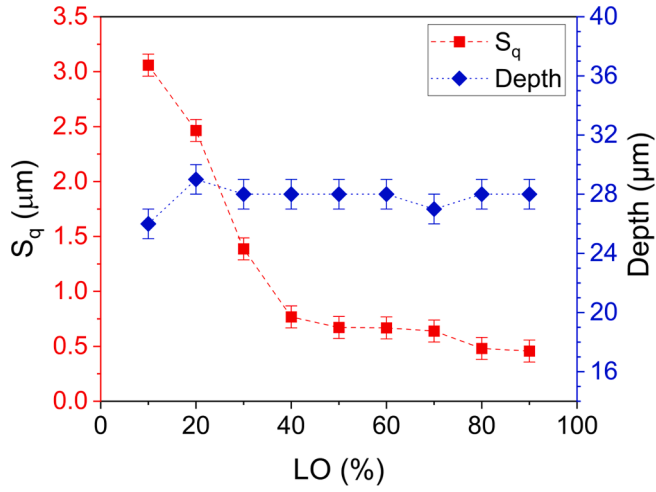
Fig. 7 shows that in the range of laser parameters investigated in the present work the milled depth increases linearly with the incident laser peak fluence F_0. A linear regression analysis of the data (blue solid line) yields a depth-to-fluence ratio of $21.7 \pm 0.8\,\mu\text{m}/(\text{J/cm}^2)$.

A strong dependence of the surface roughness S_q on the incident laser fluence can also be noticed from Fig. 7. LiNbO$_3$-based microfluidic devices [18,19] and microresonators [20,21] typically require microstructures with dimensions in the order of hundreds of μm and surface roughness below 1μm. Based on this consideration, a trade-off between the surface roughness and the control over the milled depth was achieved at a peak fluence of $1.66\,\text{J/cm}^2$, which was kept fixed for the rest of the investigation.

Subsequently, the influence of the scanning line overlap LO, determined by the hatch spacing h as described by Eq. (5), was investigated. The values of h examined ranged from 3.2 to 28.8 μm, corresponding to scanning line overlaps from 90% to 10%, employing a single cross-hatch scanning strategy, as illustrated in Fig. 3(a). For each h value, the scanning velocity v_s was calculated using Eq. (5), while keeping fixed the number of pulses per spot N_P^{2D} at 100. It is worth noticing that the scanning line overlap LO does not impact the milled depth, which remains constant at 27.8 ± 0.8 μm, but significantly affects the surface roughness, as shown in Fig. 8.
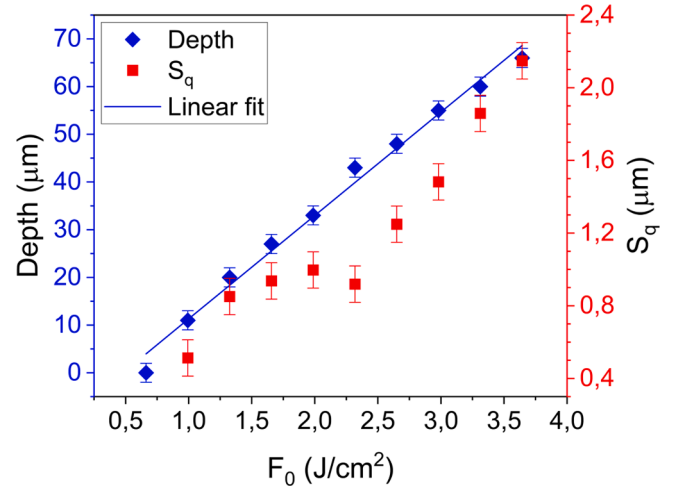
Fig. 7. Milled depth (blue diamonds) and surface roughness S_q (red squares) versus the incident laser peak fluence with 50 pulses per spot at repetition frequency $f_r = 10$ kHz. The blue solid line represents the best-fit linear regression model. The ablation was performed with a single scanning loop at fixed scanning line overlap $LO = 50\%$ and pulses per spot $N_P^{2D} = 100$. (For interpretation of the references to colour in this figure legend, the reader is referred to the web version of this article.)

Fig. 6. DIC optical micrographs of three representative craters ablated with $N = 500$ and $E_p = 20\,\mu$J at: (**a**) 1 kHz, (**b**) 10 kHz and (**c**) 100 kHz.
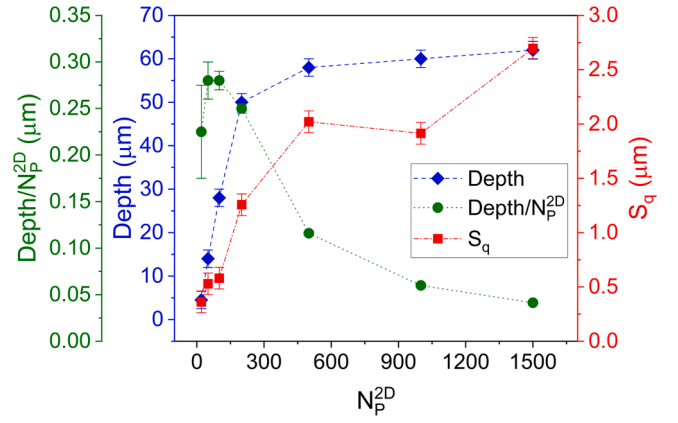
Fig. 8. Surface roughness S_q (red squares) and milled depth (blue diamonds) versus the scanning line overlap *LO*. Data points are connected by straight lines for better visualization. The micromilling was performed with a single cross-hatch scanning loop at fixed repetition frequency f_r (10 kHz), peak fluence F_0 (1.66 J/cm²), and number of pulses per spot N_P^{2D} (100). (For interpretation of the references to colour in this figure legend, the reader is referred to the web version of this article.)

Fig. 9 provides a comparison of the surface morphology between three representative cases of *LO* = 10%, 50% and 90%. The micrographs indicate that the microstructure's periodicity across the micromilled areas is given by the hatch spacing *h*, denoting the significance of this parameter in influencing surface quality [45]. A surface roughness of $0.5 \pm 0.1 \, \mu m$ was achieved with a scanning line overlap of 90%, corresponding to $h = 3.2 \, \mu m$. Based on this result, *LO* was kept fixed at 90% for the rest of the investigation.

The impact of the scan speed v_s on both milled depth and surface quality was also examined while keeping fixed the other parameters. However, for a more comprehensive analysis, the results are reported as a function of the number of pulses per spot N_P^{2D}. This parameter is related to the scanning speed according to Eq. (6). Fig. 10 displays the results obtained for N_P^{2D} ranging from 20 to 1500, corresponding to scan speeds ranging from 160 mm/s to 2 mm/s.

Fig. 10 shows how the milled depth rapidly increases with the number of incident pulses until a plateau is reached for $N_P^{2D} > 300$. This behavior could be better understood by examining the pulse ablation


Fig. 10. Milled depth (blue diamond), milled depth per pulse (green circles) and surface roughness S_q (red squares) versus the number of pulses per spot N_P^{2D}. Data points are connected by straight lines for better visualization. The micromilling was performed with a single scanning loop at fixed repetition frequency $f_r = 10$ kHz, peak fluence $F_0 = 1.66$ J/cm² and scanning line overlap $LO = 90\%$. (For interpretation of the references to colour in this figure legend, the reader is referred to the web version of this article.)

efficiency (green circles), i.e. the milled depth per incident pulse, which peaks around $N_P^{2D} = 50$ before rapidly decreasing. The observed saturation plateau could be ascribed to the heat accumulation which leads to material melting and redeposition [46] and prevents further material removing. This hypothesis is supported by the sharp rise in surface roughness for $N_P^{2D} > 100$, corresponding to $v_s < 32$ mm/s. Consequently, the scanning speed was set at 160 mm/s, corresponding to $N_P^{2D} = 20$, in order to achieve the lowest surface roughness of $0.4 \pm 0.1 \, \mu m$. This speed was maintained fixed throughout the remainder of the investigation.

The fit in Fig. 11(a) shows that the milled depth is proportional to the number of scanning loops $L^{\#}$. This correlation underscores the precision achievable in controlling micromilled depth using the selected laser parameters, with each scanning loop resulting in a consistent step size of $6.0 \pm 0.1 \, \mu m$. Furthermore, the morphological analysis confirmed that the surface finish remained nearly unchanged with the varying number of loops, maintaining a surface roughness S_q of $0.6 \pm 0.1 \, \mu m$. Fig. 11(b) reports the transverse section of four representative channels micromilled with increasing number of scanning loops $L^{\#}$, from 2 to 24.

The transverse section of the milled areas reveals a wall tapering, a distinctive feature resulting from the Gaussian intensity distribution of the focused laser beam used for the milling process. The tapering results
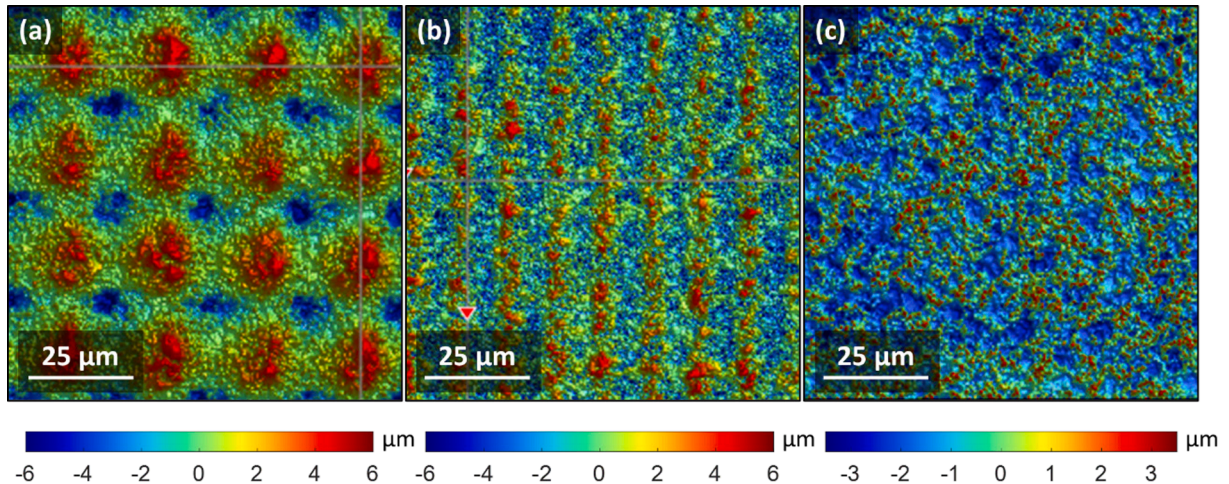
Fig. 9. Optical profilometer micrographs of the surface morphologies obtained at scanning line overlaps *LO* of: (**a**) 10%, (**b**) 50% and (**c**) 90%. The micromilling was performed with a single cross-hatch scanning loop at fixed repetition frequency f_r (10 kHz), peak fluence F_0 (1.66 J/cm²), and number of pulses per spot N_P^{2D} (100).
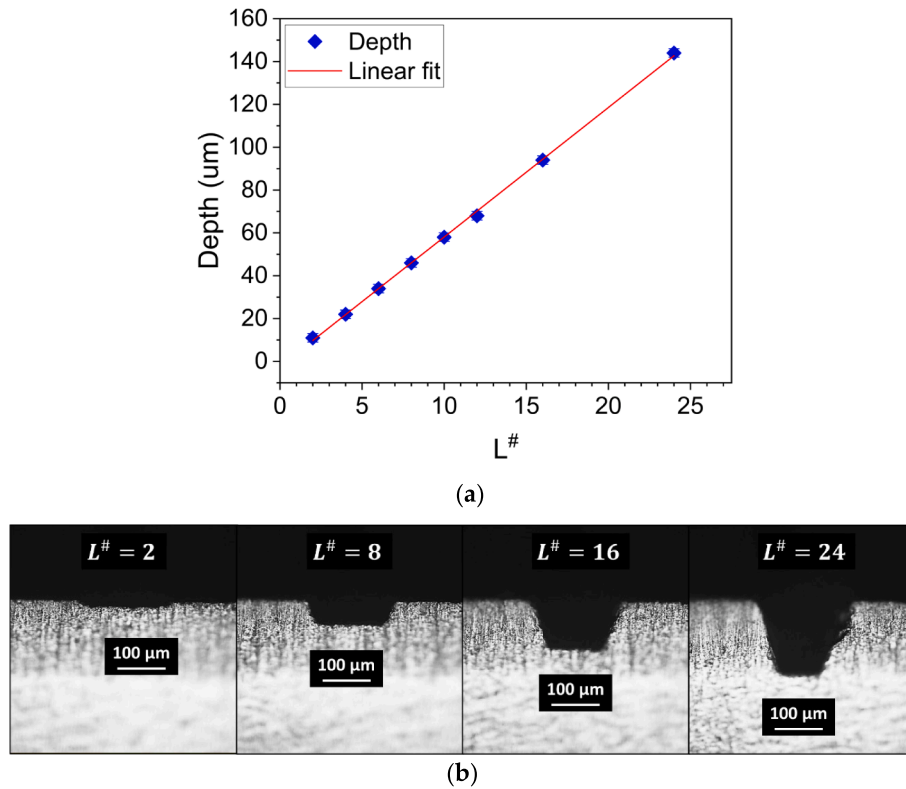
Fig. 11. (**a**) Milled depth dependence on the number of scanning loops $L^{\#}$, a linear regression model (in red) was applied. (**b**) DIC optical micrographs of the transverse section of micromilled areas with increasing number of scanning loops $L^{\#}$. The micromilling was performed at fixed repetition frequency $f_r = 10\,\text{kHz}$, peak fluence $F_0 = 1.66\,\text{J/cm}^2$, scanning line overlap $LO = 90\%$ and scanning velocity $v_s = 160\,\text{mm/s}$. (For interpretation of the references to colour in this figure legend, the reader is referred to the web version of this article.)

in an approximate $20°$ inclination of the walls, which prevents from obtaining a perfectly rectangular section.

4. Conclusions

In this work, a systematic investigation about the laser ablation of $128°$ Y-cut LiNbO$_3$ employing multi-pulse fs-laser ablation was presented.

The multi-pulse surface ablation threshold fluence $F_{th}(N)$ was measured at increasing number of pulses N, while also examining the impact of different repetition frequency f_r. It was observed that the multi-shot threshold fluence decreases as the number of incident laser pulses increases, regardless of the repetition frequency. This trend aligns with the cumulative effects associated with the incubation model and was best described by a power model.

The measured value for the single pulse ablation threshold $F_{th,1}$ was consistent with values reported in existing literature for LiNbO$_3$. The incubation coefficient S^* was nearly constant across all the repetition frequencies. Conversely, the asymptotic ablation threshold $F_{th,\infty}$ remained constant at low repetition frequencies (i.e., 1-10 kHz) but decreased in the 100 kHz regime. In the latter range, the incubation mechanisms are enhanced, leading to a further reduction in the ablation threshold.

A systematic investigation was conducted to analyze the impact of various key parameters, including pulse peak fluence F_0 and the total number of pulses per spot N_P^{2D}, on the fs-laser micromilling process of LiNbO$_3$. The study revealed a direct correlation between the milled depth and the surface roughness of the processed areas with F_0. At constant pulse peak fluence, it was observed that the milled depth per incident pulse reached its maximum around $N_P^{2D} = 50$ before rapidly decreasing for $N_P^{2D} > 300$ due to material melting and redeposition

resulting from increased heat accumulation. Maintaining a constant number of N_P^{2D} allowed to adjust the surface roughness by varying either the hatch spacing h or the scanning velocity v_s without affecting the milled depth. This approach allowed to achieve precise control over the milled depth while maintaining a surface roughness below $1\,\mu\text{m}$, a crucial requirement for the microfabrication of MEMS devices and microfluidic systems.

The findings outlined in this study offer valuable insights into the fs-laser processing of $128°$ Y-cut LiNbO$_3$ but could be extended to other hard and brittle transparent materials known known to be difficult to machine.

CRediT authorship contribution statement

Felice Alberto Sfregola: Writing – original draft, Visualization, Investigation, Formal analysis, Conceptualization. **Raffaele De Palo:** Writing – original draft, Visualization, Investigation, Formal analysis. **Caterina Gaudiuso:** Writing – review & editing. **Francesco Paolo Mezzapesa:** Writing – review & editing. **Pietro Patimisco:** Writing – review & editing, Supervision. **Antonio Ancona:** Writing – review & editing, Formal analysis. **Annalisa Volpe:** Writing – review & editing, Visualization, Supervision, Formal analysis, Conceptualization.

Declaration of competing interest

The authors declare that they have no known competing financial interests or personal relationships that could have appeared to influence the work reported in this paper.

Data availability

Data will be made available on request.

References

[1] R.S. Weis, T.K. Gaylord, Lithium niobate: Summary of physical properties and crystal structure, Applied Physics A 37 (4) (1985) 191–203, https://doi.org/10.1007/BF00614817.

[2] V.Y. Shur, Lithium niobate and lithium tantalate-based piezoelectric materials, Advanced Piezoelectric Materials: Science and Technology (Jan. 2010) 204–238, https://doi.org/10.1533/9781845699758.1.204.

[3] M. Toda, M. Thompson, A. Sirven, C. Nordin, "The influence of oil density and viscosity on the behavior of a lithium niobate tuning fork cantilever", IEEE International Ultrasonics Symposium, IUS (2012), https://doi.org/10.1109/ULTSYM.2012.0268.

[4] M. Gonzalez, G. Ham, A. Al Haddad, G. Bernero, M. Deffenbaugh, Downhole viscosity measurement platform using tuning fork oscillators, *2015 IEEE SENSORS - Proceedings*, Dec. (2015), https://doi.org/10.1109/ICSENS.2015.7370266.

[5] A.F.P. Cantatore, et al., Lithium Niobate – enhanced photoacoustic spectroscopy, Photoacoustics (2023) 100577, https://doi.org/10.1016/J.PACS.2023.100577.

[6] W.-K. Tseng, J.-L. Lin, W.-C. Sung, S.-H. Chen, G.-B. Lee, Active micro-mixers using surface acoustic waves on Y-cut 128° LiNbO3, Journal of Micromechanics and Microengineering 16 (3) (Feb. 2006) 539, https://doi.org/10.1088/0960-1317/16/3/009.

[7] C. Wood, S. Evans, J. Cunningham, R. O'Rorke, C. Wälti, A. Davies, Alignment of particles in microfluidic systems using standing surface acoustic waves, Appl Phys Lett 92 (Aug. 2008) 44104, https://doi.org/10.1063/1.2838748.

[8] D. Huo, Z.J. Choong, Y. Shi, J. Hedley, Y. Zhao, Diamond micro-milling of lithium niobate for sensing applications, Journal of Micromechanics and Microengineering 26 (9) (Sep. 2016) 095005, https://doi.org/10.1088/0960-1317/26/9/095005.

[9] Z.Y.A. Al-Shibaany, J. Hedley, D. Huo, Z. Hu, Micromachining Lithium Niobate for Rapid Prototyping of Resonant Biosensors, IOP Conf Ser Mater Sci Eng 65 (Jul. 2014) 012030, https://doi.org/10.1088/1757-899X/65/1/012030.

[10] M. Sridhar, D.K. Maurya, J. Friend, L. Yeo, Focused ion beam milling of microchannels in lithium niobate, Biomicrofluidics 6 (Nov. 2012) 12819–1281911, https://doi.org/10.1063/1.3673260.

[11] P. Sengupta, K. Khanra, A. Roy Chowdhury, P. Datta, Lab-on-a-chip sensing devices for biomedical applications. 10.1016/B978-0-08-102420-1.00004-2.

[12] J. Mur, A. Mikelj, B. Podobnik, R. Petkovšek, Precision fabrication of flexible microfluidic circuits using direct laser rapid prototyping solution, Journal of Micromechanics and Microengineering 30 (11) (Nov. 2020) 115005, https://doi.org/10.1088/1361-6439/aba63f.

[13] K. Sugioka, Y. Hanada, K. Midorikawa, Three-dimensional femtosecond laser micromachining of photosensitive glass for biomicrochips, Laser Photon Rev 4 (3) (Apr. 2010) 386–400, https://doi.org/10.1002/LPOR.200810074.

[14] M. Terakawa, Femtosecond Laser Processing of Biodegradable Polymers, Applied Sciences 8 (Aug. 2018) 1123, https://doi.org/10.3390/app8071123.

[15] F. Piscitelli, R. De Palo, A. Volpe, Enhancing Adhesion on fibre-reinforced composite by femtosecond laser texturing, Coatings 13 (5) (May 2023) 928, https://doi.org/10.3390/COATINGS13050928.

[16] D. Karnakis, G. Rutterford, M. Knowles, T. Dobrev, P. Petkov, and S. Dimov, "High quality laser milling of ceramics, dielectrics and metals using nanosecond and picosecond lasers," *Proc. SPIE 6106, Photon Processing in Microelectronics and Photonics*, pp. 610604–61060411, Aug. 2006.

[17] A. Volpe, C. Gaudiuso, L. Di Venere, F. Licciulli, F. Giordano, A. Ancona, Direct femtosecond laser fabrication of superhydrophobic aluminum alloy surfaces with anti-icing properties, Coatings 10 (6) (2020), https://doi.org/10.3390/coatings10060587.

[18] G. Pozza, et al., T-junction droplet generator realised in lithium niobate crystals by laser ablation", Optofluidics, Microfluidics and Nanofluidics 1 (1) (Nov. 2014), https://doi.org/10.2478/OPTOF-2014-0003.

[19] G. Bettella, et al., Lithium niobate micromachining for the fabrication of microfluidic droplet generators, Micromachines (basel) 8 (6) (Jun. 2017) 185, https://doi.org/10.3390/MI8060185.

[20] J. Lin, et al., Fabrication of high-Q lithium niobate microresonators using femtosecond laser micromachining, Scientific Reports 5 (1) (Jan. 2015) 1–4, https://doi.org/10.1038/srep08072.

[21] L.-K. Chen, Y.-F. Xiao, On-chip lithium niobate microresonators for photonics applications, Science China Physics, Mechanics Astronomy 63 (2) (Oct. 2019) 1–2, https://doi.org/10.1007/S11433-019-9453-3.

[22] E. Gamaly, A. Rode, B. Luther-Davies, Ablation of solids by femtosecond lasers: Ablation mechanism and ablation thresholds for metals and dielectrics, Phys Plasmas 9 (Aug. 2001), https://doi.org/10.1063/1.1447555.

[23] E. Mazur, Femtosecond laser micromachining in transparent Materials, Adv. Photonics Renew. Energy (2010) BWB4, https://doi.org/10.1364/BGPP.2010.BWB4.

[24] H. Chen, X. Chen, Y. Zhang, Y. Xia, Ablation induced by single-and multiple-femtosecond laser pulses in lithium niobate, Laser Phys 17 (12) (Dec. 2007) 1378–1381, https://doi.org/10.1134/S1054660X07120079.

[25] Q. Meng, B. Zhang, S. Zhong, L. Zhu, Damage threshold of lithium niobate crystal under single and multiple femtosecond laser pulses: theoretical and experimental study, Applied Physics A 122 (6) (2016) 582, https://doi.org/10.1007/s00339-016-0120-x.

[26] L.E.L. Fissi, V. Xhurdebise, L.A. Francis, Effects of laser operating parameters on piezoelectric substrates micromachining with picosecond laser, Micromachines 6 (1) (2015) 19–31, https://doi.org/10.3390/MI6010019.

[27] J.M. Liu, Simple technique for measurements of pulsed Gaussian-beam spot sizes, Opt. Lett. 7 (5) (May 1982) 196–198, https://doi.org/10.1364/OL.7.000196.

[28] F. Marinello, A. Pezzuolo, Application of ISO 25178 standard for multiscale 3D parametric assessment of surface topographies, IOP Conf. Ser. Earth Environ. Sci. 275 (1) (May 2019), https://doi.org/10.1088/1755-1315/275/1/012011.

[29] G. Schnell, U. Duenow, H. Seitz, Effect of laser pulse overlap and scanning line overlap on femtosecond laser-structured Ti6Al4V surfaces, Materials 13 (4) (2020), https://doi.org/10.3390/ma13040969.

[30] G. Giannuzzi, et al., Short and long term surface chemistry and wetting behaviour of stainless steel with 1D and 2D periodic structures induced by bursts of femtosecond laser pulses, Appl Surf Sci 494 (Nov. 2019) 1055–1065, https://doi.org/10.1016/J.APSUSC.2019.07.126.

[31] C. Marco, et al., Surface Properties of Femtosecond Laser Ablated PMMA, ACS Appl Mater Interfaces 2 (Sep. 2010) 2377–2384, https://doi.org/10.1021/am100393e.

[32] Y. Jee, M.F. Becker, R.M. Walser, Laser-induced damage on single-crystal metal surfaces, J. Opt. Soc. Am. B 5 (3) (Mar. 1988) 648–659, https://doi.org/10.1364/JOSAB.5.000648.

[33] R. De Palo, A. Volpe, C. Gaudiuso, P. Patimisco, V. Spagnolo, A. Ancona, Threshold fluence and incubation during multi-pulse ultrafast laser ablation of quartz, Opt Express 30 (Aug. 2022), https://doi.org/10.1364/OE.475592.

[34] F. Di Niso, C. Gaudiuso, T. Sibillano, F. Mezzapesa, A. Ancona, P. Lugarà, Role of heat accumulation on the incubation effect in multi-shot laser ablation of stainless steel at high repetition rates, Opt Express 22 (Nov. 2014) 12200–12210, https://doi.org/10.1364/OE.22.012200.

[35] B. Neuenschwander, et al., Factors controlling the incubation in the application of ps laser pulses on copper and iron surfaces, in: X. Xu, G. Hennig, Y. Nakata, S. W. Roth (Eds.), Laser Applications in Microelectronic and Optoelectronic Manufacturing (LAMOM) XVIII, SPIE, 2013, p. 86070D, https://doi.org/10.1117/12.2004136.

[36] J. Bonse, S. Baudach, J. Krüger, W. Kautek, M. Lenzner, Femtosecond laser ablation of silicon–modification thresholds and morphology, Applied Physics A 74 (Aug. 2002) 19–25, https://doi.org/10.1007/s003390100893.

[37] A. Rosenfeld, M. Lorenz, R. Stoian, D. Ashkenasi, Ultrashort-laser-pulse damage threshold of transparent materials and the role of incubation, Applied Physics A 69 (1) (1999) S373–S376, https://doi.org/10.1007/s003390051419.

[38] P.P. Rajeev, et al., Memory in Nonlinear Ionization of Transparent Solids, Phys Rev Lett 97 (25) (Dec. 2006) 253001, https://doi.org/10.1103/PhysRevLett.97.253001.

[39] C. Schaffer, A. Brodeur, E. Mazur, Laser-Induced Breakdown and Damage in Bulk Transparent Materials Induced by Tightly Focused Femtosecond Laser Pulses, Measurement Science & Technology - MEAS SCI TECHNOL 12 (Aug. 2001), https://doi.org/10.1088/0957-0233/12/11/305.

[40] S.S. Mao, et al., Dynamics of femtosecond laser interactions with dielectrics, Applied Physics A 79 (7) (2004) 1695–1709, https://doi.org/10.1007/s00339-004-2684-0.

[41] F. Costache, S. Eckert, J. Reif, Near-damage threshold femtosecond laser irradiation of dielectric surfaces: Desorbed ion kinetics and defect dynamics, Applied Physics A 92 (Sep. 2008) 897–902, https://doi.org/10.1007/s00339-008-4632-x.

[42] D. Ashkenasi, M. Lorenz, R. Stoian, A. Rosenfeld, Surface damage threshold and structuring of dielectrics using femtosecond laser pulses: the role of incubation, Appl Surf Sci 150 (1–4) (Aug. 1999) 101–106, https://doi.org/10.1016/S0169-4332(99)00228-7.

[43] J. Hernandez-Rueda, D. Puerto, J. Siegel, M. Galvan-Sosa, J. Solis, Plasma dynamics and structural modifications induced by femtosecond laser pulses in quartz, Appl Surf Sci 258 (23) (Sep. 2012) 9389–9393, https://doi.org/10.1016/j.apsusc.2011.12.020.

[44] H. Varel, D. Ashkenasi, A. Rosenfeld, M. Wähmer, E.E.B. Campbell, Micromachining of quartz with ultrashort laser pulses, Appl. Phys. A 65 (1997) 367–373.

[45] K.L. Wlodarczyk, et al., Investigation of an interlaced laser beam scanning method for ultrashort pulse laser micromachining applications, J Mater Process Technol 285 (Nov. 2020), https://doi.org/10.1016/J.JMATPROTEC.2020.116807.

[46] F. Fraggelakis, et al., Texturing metal surface with MHz ultra-short laser pulses, Optics Express 25 (15) (Jul. 2017) 18131–18139, https://doi.org/10.1364/OE.25.018131.